Technische
Universität
München

Walther-Meißner
Institut

Bayerische
Akademie
der Wissenschaften

Electro-magnetic simulation of transmission-line-based designs of RE-doped YSO crystals for optimized spin-ensemble to microwave coupling

---

Bachelor theses
Noah Weinhold

Supervisor: Prof. Dr. Rudolf Gross
Advisor: Dr. Nadezhda Kukharchyk
Garching – September 12, 2021

Contents

1 Introduction and motivation

The birth of quantum information, which combines quantum computing (QC) and quantum communication, can be dated back to the 1990s. As quantum information (QI) promises huge processing capacity [1], massive effort in research has been invested in its development. There are many platforms considered as hardware for QI, such as superconducting qubits, artificially trapped ions, cold atoms, defect centers or rare earth (RE) ions in solids [2]. Every platform is better or worse suited for certain tasks, namely storing, processing and transmitting quantum information. Hybrid systems, consisting of several different components represent a promising way of building quantum information devices [3]. Spin ensembles, for example, are well suited for long-living quantum memories. RE spin ensembles are particularly interesting, since the ions have transitions in the optical and microwave regime, which makes them especially versatile. In addition they are relatively robust against external influences and posses very good coherence properties [2]. Therefore the overall aim of the project is to realize a quantum memory system with RE doped yttrium orthosilicate in a transmission line based design.

The topic of this thesis is the optimization of the transmission properties of a coaxial, a coplanar and a twinwire designs using electromagnetic (EM) simulations with CST. Efficient quantum memories require good and coherent spin-ensemble to EM-field coupling, which depends on the field strength. Therefore it is important to create as strong and homogeneously distributed fields as possible. This can be achieved by minimized reflections and maximized transmission, denoted by S_{11} and S_{21}. Therfore the simulations are oriented towards obtaining the highest S_{21} parameter possible in a frequency range from 1 GHz to 7 GHz.

In the theory part, different quantum memory techniques are the first topic that will be discussed, since it is the motivation behind the project. Then the theoretical background to the EM simulations will be given in the transmission line (TL) theory section. The properties of YSO, the difference between resonators and TLs and the coupling of spin ensembles to EM fields will round up the theory part of the thesis. In the experimental part the simulation processes and results are presented.

2 Theory

2.1 Quantum memory systems

Generally a quantum memory is a quantum system that is able to coherently and reliably store and retrieve quantum states. There is a number of different types of quantum memories, which differ in the type of state stored (e.g. single photon states, squeezed states, etc.), the operating frequency domains (e.g. optical, IR, microwave), the interaction type (transmission coupling or resonator), etc. In order to compare these different systems, the next section introduces performance criteria on which they can be rated. Afterwards a few different relevant memory protocols based on spin ensembles and NV-centers are presented.

2.1.1 Performance criteria

In order to compare and rate the performance of a quantum memory it is necessary to define criteria on which the performance is defined:

1. The first criterion is the ***fidelity***: In general terms it describes the overlap of the quantum states of the memory and the retrieved state but the exact definition depends on the approach chosen. For single photon memories it describes the overlap of the wave packet from input and output photon. This is also called conditional fidelity because it depends on the re-emission of a photon. In contrast, for purposes that need to store general states of light, unconditional fidelity is the appropriate notion. For certain applications purity might be the better criterion than fidelity. For processes where the output is linked to the input via a known unitary transformation, this would not harm the stored information, but the fidelity in such cases would be bad.

2. The notion of ***efficiency*** is best defined for single photon memories. In this case it describes the probability to reemit a stored photon. The efficiency for atomic ensembles is usually close to one due to interference effects, whereas it is low for single atomic systems. For memories that are meant to store general states of light the efficiency is not well defined. In this case unconditional fidelity is the better criterion.

3. ***Storage time*** is another core criteria, that determines drastically the circle of applications the memory can be used for. It describes the duration at which a quantum mechanical state can be reliably maintained. It is typically directly related to the coherence time. The minimum storage time needs to be at least as long as the duration of the entanglement creation, which lies in the range of seconds for realistic devices. Long storage times are important for many devices, but especially for long distance quantum repeaters it is crucial for good performance.

4. The ***temporal bandwidth*** describes the duration between the beginning of a storage process and the next point in time at which the next process can be started. It will define the operational speed of a memory as it determines the achievable repetition rate and multiplexing potential.

5. Another important characteristic of a memory is its ***modality***, so whether it is a single or multi-mode memory. The capacity to store multiple photon modes is a given characteristic for most ensembles and has a huge influence on the achievable repetition rate. It is therefore of great interest to know the number of photons that can be stored.

6. The last criterion is the wavelength range (IR, Microwave, etc.) at which a memory is operating. Especially for long distance quantum communication, it is important to use wavelengths at which the absorption losses in optical fibers are minimal. A good example here would be Erbium, having transitions in IR $\simeq$1550 nn, which lies in the Telecom C band of optical fibres [4].

2.1.2 Physical requirements

In the following paragraph the focus lies on the physical requirements to get good memories with respect to the figures of merit discussed in the abstract above. Since the criteria are usually interdependent and it is therefore not possible to meet each of them at a high level simultaneously, only the two requirements needed for both good efficiency/fidelity on one hand and long storage times on the other hand are discussed. The first one is the notion of light-matter coupling: For memories relying on the absorption and re-emission of light, the coupling is defined as the probability to absorb the light. In the case of atomic ensembles (e.g. gases or solids) good coupling is reached by having high optical depth. In a cavity the finesse plays the role of optical depth. For applications where the memory excitation is created by the emission of a photon, good coupling is related to the probability of emitting a photon into a well defined mode.

The second requirement is coherence. Its influence on the actual memory time varies between the different approaches. For the case of single atomic systems decoherence influences the fidelity but not the efficiency, for protocols based on collective effects, such as controlled reversible inhomogeneous broadening (CRIB), it is the other way around [4].

2.1.3 Realization with Rare-earth ions in solids

In this chapter, the possible realizations of a quantum memory using rare-earth (RE) ion ensembles in solids are discussed. RE ions are very attractive due to the long coherence times of their 4f-4f transition, which is in the range of seconds at cryogenic temperatures and makes them well suited for transferring photonic states to atomic states. However, the narrow homogeneous linewidth, rooting in the long coherence time, gets overshadowed by inhomogeneous broadening once doped into solids, which causes inhomogeneous dephasing of the coherent states. The storage protocols presented in this thesis, are based on the absorption and re-emission of photons using photon-echo effects, which relies on the aforementioned dephasing. Two promising protocols are the aforementioned ***controlled reversible inhomogeneous broadening (CRIB)*** and the ***atomic frequency comb (AFC)*** [4].

In the following, the scheme of controlled reversible inhomogeneous broadening (CRIB) is described in more detail. This method intentionally broadens and refocuses the, in theory narrow, absorption linewidth using the linear Stark-effect. The Stark-effect was discovered by J.Stark in 1913 [5]. He discovered that the energy levels of atoms experience an additional splitting in an external electric field, due to the extra Term $H' = eEz$ added to the Hamiltonian, similar to the Zeemann effect in an external magnetic field. So by applying an external electrical field gradient the atoms accumulate a detuning Δ with a phase $e^{-i\Delta\tau}$ after a time $t = \tau$. By inverting the polarity of the field the atoms invert their detuning and after a time $t = 2\tau$, they have gained a phase $e^{i\Delta\tau}$, which leads to a rephasing of the spin ensemble and the emission of a light pulse. The efficiency η_{CRIB} of this protocol is given by [4]:

$$\eta_{CRIB} = (1 - e^{-\bar{d}})^2 sinc^2(\gamma_0 t), \tag{1}$$

whith $\bar{d} = d\gamma_0/\gamma$ where d is the initial optical depth, γ_0 is the initial linewidth, γ is the broadened linewidth and t is the storage time of the excited state. As shown

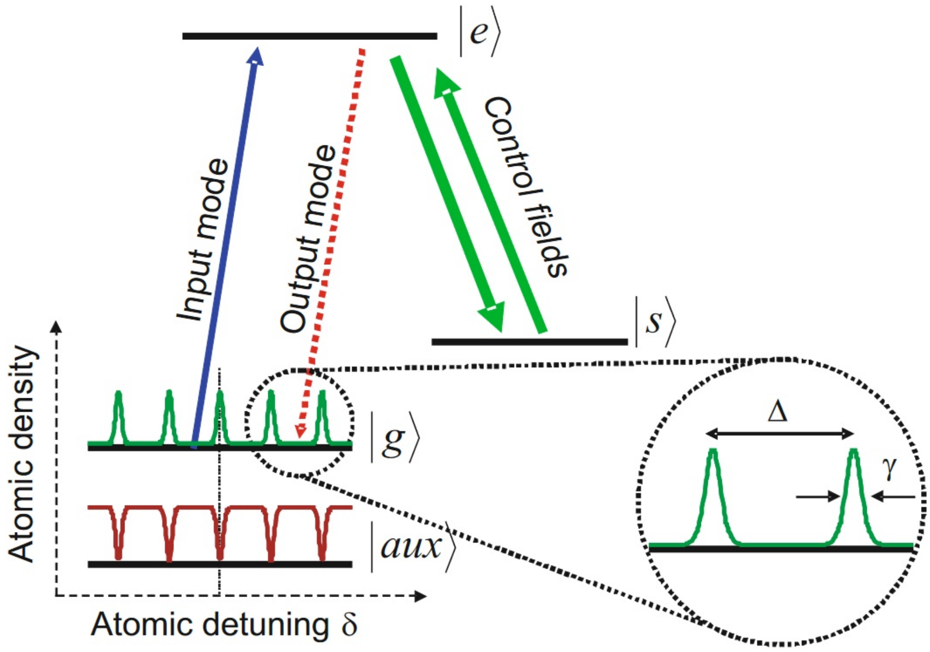

Figure 1: A schematic of the AFC protocol is presented here, with $|g\rangle$, $|aux\rangle$, $|e\rangle$ and $|s\rangle$ denoting the ground, auxilary, excited and long living ground state, respectively. The peaks in the frequency comb in $|g\rangle$, have a width γ and a seperation Δ. The figure is taken from [4].

in the equation above, the efficiency consists of two factors: The first one is related to the square of the absorption probability, the second one describes the dephasing caused by the initial linewidth γ_0 and its exact form depends on the actual shape of the line. According to the equation 1, the more broadening is added and the longer the signal is stored, the less efficient the storage becomes. If one wants to increase the storage time, once absorbed, the pulse can be transferred to a lower-lying state, e.g. to the hyperfine multiplet of the groundstate. Here, the only limitation is given by the decoherence. In order to store multiple modes, very high optical depths are required for the CRIB scheme, therefore another protocol exists which is better suited for mode multiplexing using atomic frequency combs (AFC). It is presented in the following paragraph [4].

The AFC is created using spectral hole burning techniques, which allows ”to isolate a sub-ensemble of atoms whose different hyperfine transitions can be unambiguously excited” [2]. Transferring the atoms from the ground state $|g\rangle$ to an auxiliary storage level $|aux\rangle$ a narrow absorption line can be created by transferring back atoms within a small frequency range from $|aux\rangle$ to $|g\rangle$ (fig. 1). By transferring back atoms at different frequencies, one obtains a frequency comb, of small lines with width γ separated by Δ. The idea is, that now a single photon gets collectively absorbed and its state is converted to atomic excitations. The atoms at different frequencies will start to dephase, but due to the periodic structure of the comb, they will rephase after $t = 2\pi/\Delta$ and therefore emit a photon that, for example, can be collected in a readout process. For longer storage times, the excitation can be transferred to a ground state $|s\rangle$ with longer life-times, where the information is stored as a spin wave. Assuming negligible decoherence for $|s\rangle$ and Gaussian lineshapes, the efficiency η_{AFC} is given by

[4]

$$\eta_{AFC} = (1 - e^{-\bar{d}})^2 e^{-\frac{7}{F^2}}, \tag{2}$$

with the effective optical depths $\bar{d} = d/F$ and the finesse of the AFC $F = \Delta/\gamma$. Consequently, the efficiency converges to unity for large d and F. The number of modes that can be stored is proportional to the number of peaks in the comb and independent of the optical depth.

Now we shall have a brief overview of the figures of merit regarding the memories using RE doped solids. Fidelities above 95 % have been reached in experiments so far, since it isn't affected by decoherence processes. Theoretically efficiencies up to 100 % should be achievable, however only 45 % for the CRIB and 34 % for the AFC have been experimentally realized so far. The storage time is mainly limited by the linewidth of the excited state, with a theoretical maximum given by the homogeneous linewidth. So far storage times of tens of microseconds have been reached. This can be increased significantly by transferring the excitation to long living ground states. For the AFC the bandwidth depends largely on the spacing of the peaks and performances of several hundreds of MHz have been realized. The wavelength at which the protocol can be operated is determined by the transition frequency of the ion used and can range from 580 nm for Eu to 1530 nm for Er, the latter is the only element suited for quantum communication and quantum repeaters because only large wavelength are sent through optical fibers [4].

2.1.4 NV centers in diamond

Even though this technique has no application in the designs used in our approach, I want to give you a brief overview over quantum memories based on nitrogen vacancy (NV) defects in diamond, because they have gained huge popularity over the last decade.

Diamond is a form of carbon, that has a crystal structure called diamond cubic. Here every atom has 4 adjacent neighbour atoms that all have an angle of 109, 5° to one another. A NV center is an point defect, where one carbon atom is replaced by a nitrogen atom and a nearest neighbor atom is replaced by a lattice vacancy (Fig. 2). They gained their popularity because, even at room temperature, the NV centers have very narrow and stable optical excitation and emission lines and the stiff lattice of the diamond leads to long coherence times of electron and nuclear spins.

The defect forms a three level system with a ground state triplet (S=1), an excited state triplet and an intermediate state singlet (S=0) with respective hyperfine structure. This allows the usage of AFC type techniques, with long term storage possibilities, in the range of microseconds up to seconds, by exploiting electron and nuclear sub spin levels[4].

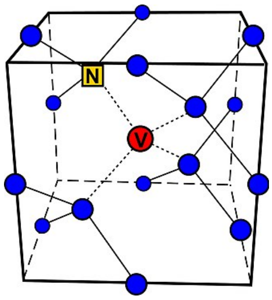

Figure 2: Schematic of a NV center in diamond. Blue dot = carbon atom. This figure is taken from [6].

Another approach is to couple the strongly allowed optical transition from the defect to a cavity. Here one can distinguish ensemble based approaches relying on electromagnetically induced transparency (EIT) like two photon resonance and single photon to defect coupling. EIT is a technique that creates a transparency window in an absorption spectrum, a shift of the peak to a slightly higher and a slightly lower frequency with an absorption of zero at the original peak, by applying couplings fields [7]. Consequently the medium gets transparent at the normal absorption frequency. But since these methods are not relevant for our experimental setup, they shall not be discussed in more detail [4].

2.1.5 Other memory types

Since there are many other ways to store and process quantum information and to dive deeper into every one of it would go beyond the scope, they shall just be mentioned quickly. Two approaches are involving gases, namely techniques relying on room temperature alkali gases with long spin polarization life time and Raman memory in atomic gases and solids. Then there are memories directly involving atoms like single optically trapped ^{87}Rb atoms on one hand and cold trapped atomic ensembles on the other hand. Finally a very different approach utilizes semiconductor nanotechnology [4].

2.2 Transmission line theory

One of the main differences between circuit and transmission line (TL) theory lies in their respective dimensions. The assumption is, that the wavelength of the electromagnetic (EM) fields is much larger than a circuit and therefore currents (I) and voltages (V) can be assumed as constant over the hole network. In contrast the dimensions of a transmission line are assumed to be in the same order as the wavelength of the EM mode and consequently I and V can vary in magnitude and phase [8].

2.2.1 Impedance calculation

Since TLs for transverse electromagnetic (TEM) always consist of at least two conductors, they are schematically often represented as two wire lines (Fig. 3a). An infinitesimal piece of it, can be modeled as a circuit with per length series resistance (R), series inductance (L), shunt conductance (G) and shunt capacitance (C) as shown in figure 3b. L represents the self inductance of the two wires, C results from their close proximity, R is due to the finite conductivity of both conductors and G involves dielectric losses in the material between the wires. The equations for I and V are then given by [8]:

$$V(z) = V_0^+ e^{-\gamma z} + V_0^- e^{\gamma z}, \tag{3}$$

$$I(z) = I_0^+ e^{-\gamma z} + I_0^- e^{\gamma z}, \tag{4}$$

$$\frac{dV(z)}{d(z)} = -(R + j\omega L)I(z), \tag{5}$$

$$\frac{dI(z)}{d(z)} = -(G + j\omega C)V(z), \tag{6}$$

$$\gamma = \sqrt{(R + j\omega L)(G + j\omega C)}. \tag{7}$$

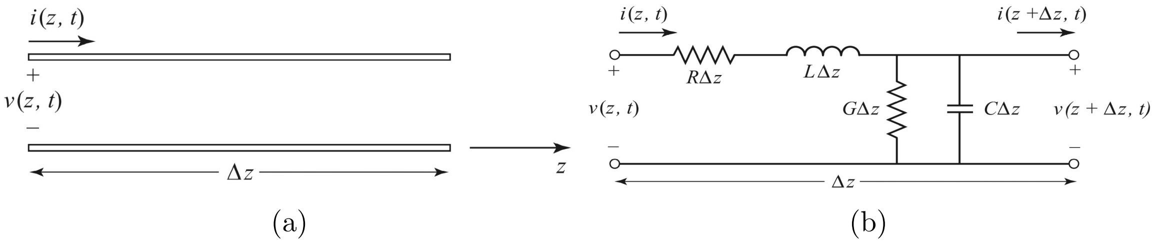

Figure 3: (a) Infinitesimal TL of length Δz with current i and voltage v, (b) Equivalent circuit. The figures are taken from [8].

The $e^{-\gamma z}$ term describes the wave propagation in positive z direction and γ denotes the complex propagation constant. By combining equations 3 - 7, the impedance Z_0 is given by the following equation [8]:

$$Z_0 = \frac{V_0^+}{I_0^+} = \frac{-V_0^-}{I_0^-} = \sqrt{\frac{R + j\omega L}{G + j\omega C}}. \tag{8}$$

In a lossless line, R and G can be set to zero. And therefore, the impedance simplifies to [8]:

$$Z_0 = \sqrt{\frac{L}{C}}. \tag{9}$$

A TL can be viewed as an number of sections of the form shown above. For the equivalent circuit ***Kirchhoff's Laws*** apply.

The calculation of the TL parameters is given by the following equations [8]:

$$L = \frac{\mu}{|I_0|^2} \int_S \vec{H} \cdot \vec{H}^* dS \frac{H}{m}, \tag{10}$$

$$C = \frac{\epsilon'}{|V_0|^2} \int_S \vec{E} \cdot \vec{E}^* dS \frac{F}{m}, \tag{11}$$

$$R = \frac{R_s}{|I_0|^2} \int_{C_1 + C_2} \vec{H} \cdot \vec{H}^* dS \frac{\Omega}{m}, \tag{12}$$

$$G = \frac{\omega \epsilon''}{|V_0|^2} \int_S \vec{E} \cdot \vec{E}^* dS \frac{S}{m}. \tag{13}$$

Here, μ and ϵ denote the complex magnetic and electric permeability, with ϵ' and ϵ'' being the real and imaginary part, R_s is the surface impedance of the conductors, I_0 and V_0 represent their respective amplitudes, S being the cross-sectional surface area of the line and $C_1 + C_2$ the integration path over boundaries of the conductors. By knowing the electric and magnetic field, one can calculate all parameters. Therefore, neglecting losses the impedance can be calculated using equation 9. This leads to the following results for coaxial (inner radius = a, outer radius = b), twinwire (radius a, distance d) and coplanar (ditance d, and width w) TLs [8]:

If one connects two sections with impedances Z_1 and Z_2 an incident wave travelling from section 1 to 2 experiences a reflection Γ that denotes the ratio of incident voltage wave amplitude to reflected voltage wave amplitude. It can be calculated with the following equation: [8]:

	coaxial	twinwire	coplanar
L	$\frac{\mu}{2\pi}\ln\frac{b}{a}$	$\frac{\mu}{\pi}\cosh^{-1}\left(\frac{d}{2a}\right)$	$\frac{d\mu}{w}$
C	$\frac{2\pi\epsilon'}{\ln b/a}$	$\frac{\pi\epsilon'}{\cosh^{-1}(d/2a)}$	$\frac{\epsilon' w}{d}$
R	$\frac{R_s}{2\pi}\left(\frac{1}{a}+\frac{1}{b}\right)$	$\frac{R_s}{\pi a}$	$\frac{2R_s}{w}$
G	$\frac{2\pi\omega\epsilon''}{\ln(a/b)}$	$\frac{\pi\omega\epsilon''}{\cosh^{-1}(d/2a)}$	$\frac{\omega\epsilon'' w}{d}$
Z_0	$\sqrt{\frac{\mu}{\epsilon'}}\frac{\ln(a/b)}{2\pi}$	$\sqrt{\frac{\mu}{\epsilon'}}\frac{\cosh^{-1}(d/2a)}{\pi}$	$\sqrt{\frac{\mu}{\epsilon'}}\frac{w}{d}$

Table 1: Transmission line parameters for a coaxial, twin-wire and coplanar TL.

$$\Gamma = \frac{V_1^-}{V_1^+} = \frac{Z_2 - Z_1}{Z_2 + Z_1}. \tag{14}$$

Since reflections are usually not wanted, it is tried to set the impedances so that $|\Gamma|$ is minimized. The optimum according to equation 14 is achieved when $Z_1 = Z_2$. Therefore all sections in the models used in this thesis are matched to $50\,\Omega$. The process of optimizing Γ between different sections of a network is called *impedance matching*.

2.2.2 Scattering matrix

In microwave network analysis, one generally takes a look at circuits with N ports. With $V_i = V_i^+ + V_i^-$ and $I_i = I_i^+ - I_i^-$ being the voltage and current wave functions of port i, exponents ± denote the incident and reflected wave, they are connected by the impedance matrix [Z] as shown in the following equation [8]:

$$\begin{pmatrix} V_1 \\ \vdots \\ V_N \end{pmatrix} = \begin{pmatrix} Z_{11} & \dots & Z_{1N} \\ \vdots & \ddots & \vdots \\ Z_{N1} & \dots & Z_{NN} \end{pmatrix} \begin{pmatrix} I_1 \\ \vdots \\ I_N \end{pmatrix}, \tag{15}$$

with

$$Z_{ij} = \left.\frac{V_i}{I_j}\right|_{I_k=0 \ for \ k\neq j} \tag{16}$$

being the transfer impedance from port i to port j when all other ports are open circuited. An important figure in microwave network analysis, is the reflection and transmission portion of an incident wave. It is described by the scattering matrix ([S] matrix), which is defined as [8]:

$$\begin{pmatrix} V_1^- \\ \vdots \\ V_N^- \end{pmatrix} = \begin{pmatrix} S_{11} & \dots & S_{1N} \\ \vdots & \ddots & \vdots \\ S_{N1} & \dots & S_{NN} \end{pmatrix} \begin{pmatrix} V_1^+ \\ \vdots \\ V_N^+ \end{pmatrix}. \tag{17}$$

A specific element can be calculated by

$$S_{ij} = \left.\frac{V_i^-}{V_j^+}\right|_{V_k^+=0 \ for \ k\neq j}. \tag{18}$$

That means, S_{ij} is given by the ratio of an incident wave created by port j and its reflection at port i. The scattering matrix can be linked to the impedance matrix in the following manner [8]:

$$[S] = ([Z] + [U])^{-1}([Z] - [U]). \tag{19}$$

With $[U]$ being the unity matrix. The models used in this thesis all have only have two ports and have a symmetric design, therefore [S] and [Z] are 2×2 matrices where entries in the same diagonal have the same value. For this reason only waves created at one port need to be analyzed. S_{11} can then be obtained by comparing the wave created at port 1 and the incident wave at port 1 created by reflections in the transmission line. Similarly S_{21} can be calculated by comparing the wave created at port 1 and comparing it to the incident wave at port 2 [8].

2.2.3 TEM fields calculation

For a good functioning quantum memory system it is also important to know how the TEM fields are propagating threw the transmission lines. All calculations are based on the Maxwell (eq. 20 - 23) and the Helmholtz (24, 25) equations. Assuming an electrostatic case and the transmission line region between the two conductors is source free they can be written as [8]:

$$\nabla \times \vec{E} = -j\omega\mu\vec{H}, \tag{20}$$
$$\nabla\vec{D} = 0, \tag{21}$$
$$\nabla \times \vec{H} = j\omega\epsilon\vec{E}, \tag{22}$$
$$\nabla\vec{B} = 0, \tag{23}$$
$$\nabla^2\vec{E} = -\omega^2\mu\epsilon\vec{E}, \tag{24}$$
$$\nabla^2\vec{H} = -\omega^2\mu\epsilon\vec{H}. \tag{25}$$

Now we set the z-axis parallel to the orientation of the transmission line of infinite length. Therefore the wave propagates along the z axis and looking at TEM waves only, the field can be assumed to be of the form [8]

$$\vec{E}(x, y, z) = \vec{E}_t(x, y)e^{-j\beta z}, \tag{26}$$
$$\vec{H}(x, y, z) = \vec{H}_t(x, y)e^{-j\beta z}, \tag{27}$$

with the index t indicating the transverse field components (along $\hat{x}$ and $\hat{y}$) and β being the propagation constant in a lossless case. Equations 20 and 22 written in each component then become [8]:

$$\beta E_y = -\omega\mu H_x, \tag{28}$$
$$\beta E_x = \omega\mu H_y, \tag{29}$$
$$\frac{\partial E_y}{\partial x} - \frac{\partial E_x}{\partial y} = 0, \tag{30}$$
$$\beta H_y = -\omega\epsilon E_x, \tag{31}$$
$$\beta H_x = \omega\epsilon E_y, \tag{32}$$
$$\frac{\partial H_y}{\partial x} - \frac{\partial H_x}{\partial y} = 0. \tag{33}$$

This leads to

$$\beta^2 E_{x,y} = \omega^2 \mu\epsilon E_{x,y}, \tag{34}$$

$$\beta = \omega\sqrt{\mu\epsilon} = k. \tag{35}$$

With $\frac{\partial^2}{\partial z^2}E_{x,y} = -\beta^2 E_{x,y}$ and $\nabla_t^2 = \frac{\partial^2}{\partial x^2} + \frac{\partial^2}{\partial y^2}$ the Laplacian operator in the transerverse dimensions, the Hemholtz equation simplifies to $\nabla_t^2 E_{x,y} = 0$. Therefore [8]

$$\nabla_t^2 \vec{E}_t(x,y) = 0 \tag{36}$$

holds true. The same results can be obtained in the same way for the magnetic field. In the electrostatic case, the electric field can be written as the gradient of a potential Φ in the following form [8]:

$$\vec{E}_t(x,y) = -\nabla_t \Phi(x,y). \tag{37}$$

Since $\nabla\vec{D} = \epsilon\nabla_t\vec{E}_t = 0$,with equation 37 the transverse Laplacian equation also holds true for Φ [8]:

$$\nabla_t^2 \Phi(x,y) = 0. \tag{38}$$

With boundary conditions the potential can be determined, and therefore with equations 37, 29 and 28 the electric and magnetic fields can be determined as well [8].

As an example the fields for a coplanar TL shall be calculated in the next paragraph. We assume, that the lower plate is grounded and located at $y = 0$ and has a width from $x = 0$ to $x = w$. The upper plate is located in a distance d above the lower plate. The boundary conditions are therefore [8]

$$\Phi(x,0) = 0, \tag{39}$$

$$\Phi(x,d) = V_0. \tag{40}$$

Since there is no variation in x, the solution of 38 has the form [8]

$$\Phi(x,y) = A + By. \tag{41}$$

Applying the boundary conditions, one obtains the constants A and B. So the potential is [8]

$$\Phi(x,y) = V_0 \frac{y}{d}. \tag{42}$$

Now the transverse electric field can be calculated with the help of equation 37. Afterwards the total electric and magnetic fields can be obtained with the help of equations 26 - 29. This leads to the following results [8]:

$$\vec{E}_t = -\hat{y}\frac{V_0}{d}, \tag{43}$$

$$\vec{E} = \vec{E}_t e^{-jkz}, \tag{44}$$

$$\vec{H} = \hat{x}\frac{V_0}{\sqrt{\mu\epsilon}d}e^{-jkz}. \tag{45}$$

In a similar way the field distributions for a coaxial line and a twinwire line can be calculated. The results are presented in the tabular 2 [8].

	E-field	H-Field
Coaxial TL	$\vec{E} = \hat{e}_\rho \frac{V_0}{\ln b/a}\frac{1}{\rho}e^{-jkz}$	$\vec{H} = \hat{e}_\phi \frac{V_0}{\sqrt{\mu\epsilon}\ln b/a}\frac{1}{\rho}e^{-jkz}$
Twinwire TL	$\vec{E} = \hat{e}_\rho \frac{V_0}{\cosh^{-1}(d/2a)}\frac{1}{\rho}e^{-jkz}$	$\vec{H} = \hat{e}_\phi \frac{V_0}{\sqrt{\mu\epsilon}\cosh^{-1}(d/2a)}\frac{1}{\rho}e^{-jkz}$

Table 2: TEM fields for coaxial and twinwire TLs.

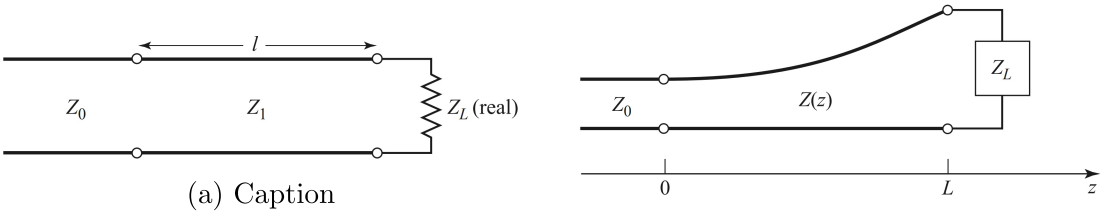

(a) Caption

(b) Caption

Figure 4: Schematics of a single section quarter-wave matching transformer (a) and an exponential tapered transmission line matching section (b). The figures are taken from [8].

2.2.4 Impedance matching

Often in microwave engineering one has to connect different devices or parts with a load impedance Z_L to a transmission line of impedance Z_0 with a connecting section. In order to optimize the transmission properties, there are several matching techniques that can be applied. A simple realization would be using a quarter wave transformer as presented in figure 4a. Here an impedance load Z_L is connected to a transmission line with Z_0 by a matching section of impedance Z_1 and length $l = \lambda_0/4$, with respect to a desired frequency f_0. Z_1 satisfies the following equation [8]:

$$Z_1 = \sqrt{Z_0 Z_L}. \tag{46}$$

This model works well if one only wants to operate at frequencies near f_0. In order to cover a greater bandwidth, for example an approach using a number of sections N with different impedances Z_i can be chosen. By increasing N, the difference between Z_i and Z_{i+1} gets smaller and smaller. But since one has finite space to work with, only a finite number of sections can be used. This arises the idea to use connections with a continuous variation of the impedance, so that $Z = Z(z)$ with $Z(0) = Z_0$ and $Z(l) = Z_L$. This approach is called *tapered line*. Its actual implementation can be realized in several different ways. The most commonly used are linear matching and exponential matching. In the first one, as the name suggests, the impedance changes linearly as described by the equation $Z(z) = Z_0 + \alpha z$. In the latter case, the matching impedance follows the relation $Z(z) = \exp\{\alpha z\}$, as illustrated by figure 4b. In both cases α is determined by the load impedance in Z_0 [8].

2.3 YSO properties

Yttrium orthosilicate (YSO) is a monoclinc material (lattice constants are presented in table 3) with the chemical formula Y_2SiO_5. It can be doped with rare earth ions, replacing one of the Yttrium atoms, which gives rise to a huge variety of applications e.g. in optical signal processing, as an active laser medium or in quantum computing.

lattice constant	a	b	c	β
value	12.402	6.6149	10.237	101.98

Table 3: The four lattice constants for YSO are listed in Å for a, b and c and in ° for β. Note that the literatur values can vary.

temperature [K]	ϵ_x	ϵ_y	ϵ_z
6	9.36000	10.90000	10.21000
296	9.59750	11.21750	10.39000

Table 4: The three entries of the permittivity tensor for YSO at temperatures 6 K and 296 K.

"The principal directions of the biaxial optical indicatrix (D_1, D_2, D_3)" [7] are perpendicular to each other, where D_3 is parallel to b and D_1 and D_2 lying in the plane of a and c, with $D_1 \angle a = 23.8°$[5]. The permittivity tensor is slightly temperature dependent. In a digonalized form, the three non-zero components (ϵ_x, ϵ_y, ϵ_z) are shown in table 4 for 6 K and 296 K [9].

2.4 Resonator and transmission line based designs

There is a number of different ways to build a quantum memory, but many of them involve either transmission line based designs or resonator based designs, or a mix of both. Therefore a quick overview over resonator properties shall be given in this section. Transmission lines have already been discussed in more detail in section 2.2 [8].

Since many microwave resonators near resonance frequency can be approximated by series or parallel RLC resonators, their properties shall be briefly discussed first. Taking a look at a circuit with a series resistance R, inductance L and capacitance C, the impedance is given by [8]

$$Z = R + j\omega L - j\frac{1}{\omega C}. \tag{47}$$

The power can then be calculated with the formula [8]

$$\begin{aligned} P &= \frac{1}{2}VI^* = \frac{1}{2}Z|I|^2 \\ &= \frac{1}{2}|I|^2(R + j\omega L - j\frac{1}{\omega C}), \qquad (48) \\ P_{loss} &= \frac{1}{2}|I|^2 R, \qquad (49) \\ W_m &= \frac{1}{4}|I|^2 L, \qquad (50) \\ W_e &= \frac{1}{4}|I|^2 \frac{1}{\omega^2 C}. \qquad (51) \end{aligned}$$

The first term represents the power dissipated by the resistance, the second and third terms respect the average magnetic (W_m) and electric (W_e) energy stored in the inductance and the capacitance. The last parameter that should be introduced is the quality factor Q. It describes the ratio of the stored energy and the lost energy per second and can be calculated with the following formula [8]:

$$Q_0 = \omega \frac{average\ energy\ stored}{energy\ loss/second} = \omega \frac{W_m + W_e}{P_{loss}}. \tag{52}$$

The index 0 denotes that this is only the quality factor of the circuit itself. At resonance frequency $\omega_0 = \frac{1}{\sqrt{LC}}$ the impedance simplifies to $Z = R$, $P = P_{loss}$, the average magnetic energy equates the average electric energy stored and therefore Q_0 simplifies to [8]

$$Q_0 = \omega_0 \frac{2W_m}{P_{loss}} = \frac{1}{\omega_0 RC}. \tag{53}$$

The quality factor here, was defined in absence of an external load caused by external circuitry and is therefore referred to as *unloaded* Q. Additional elements connected to the resonator always lower Q, due to additional losses. With Q_e denoting the external load, the loaded quality factor Q_L can be determined by [8]

$$\frac{1}{Q_L} = \frac{1}{Q_e} + \frac{1}{Q_0}. \tag{54}$$

In the case of a parallel RLC resonator the impedance changes to [8]

$$Z = \left(\frac{1}{R} + \frac{1}{j\omega L} + j\omega C \right)^{-1}. \tag{55}$$

Therefore the other parameters introduced for the series RLC resonator change to the following expressions [8]:

$$P = \frac{1}{2} V I^* = \frac{1}{2} |V|^2 \left(\frac{1}{R} + \frac{1}{j\omega L} + j\omega C \right), \tag{56}$$

$$P_{loss} = \frac{1}{2} \frac{|V|^2}{R}, \tag{57}$$

$$W_e = \frac{1}{4} |V|^2 C, \tag{58}$$

$$W_m = \frac{1}{4} \frac{|V|^2}{\omega^2 L}, \tag{59}$$

$$Q = \omega_0 RC. \tag{60}$$

Q is noted here at the resonance frequency, which does not change.
As an example a rectangular waveguide cavity resonator shall be presented briefly. For a rectangular cavity of width a, height b and length d coated with metal, only discrete modes are supported, because of the boundary condition, that the electric field must vanish on the sides of the cavity. This is expressed in the wavenumber [8]

$$k_{mnl} = \sqrt{\left(\frac{m\pi}{a} \right)^2 + \left(\frac{n\pi}{b} \right)^2 + \left(\frac{l\pi}{d} \right)^2}. \tag{61}$$

The calculation for the unloaded quality factor is complicated, so only the result for the TE_{101} mode is presented [8]:

$$Q = \frac{(kad)^3 b\sqrt{\mu\epsilon}}{2\pi^2 R_s} \frac{1}{2l^2a^3b + 2bd^3 + l^2a^3d + ad^3}. \tag{62}$$

Here, R_s denotes the surface impedance of the metal wall. According to equation 62, the energy loss of the cavity is higher for higher modes [8].

So generally speaking, the main difference between resonators and transmission lines is, that resonators mainly support only certain frequencies and transmission lines support all frequencies. Resonators have the advantage that the modes get amplified and consequently the coupling to spins gets enhanced as well (sec. 2.5). The benefit from transmission lines on the other hand lies in the fact, that the user does not need to determine in advance the exact frequencies that shall be exploited, because the design is more flexible.

2.5 Coupling of spin ensembles to the modes microwave field

To fully understand the way quantum memories operate, it is crucial to understand the interaction of spin ensembles with microwave fields. Since there are almost exclusively experiments with resonators coupling to spin ensembles, only this case shall be discussed in this section, because the coupling itself is similar for transmission line to spin ensemble coupling. The biggest difference lies only in the fact that resonators host standing waves and transmission lines carry travelling waves. This leads to slightly different mode volumes, what has an effect on the coupling rate. In the following the coupling to a single spin will be discussed, before generalizing it to an ensemble of spins.

These two cases are described by the *Jaynes-Cummings model* which was then expanded to the *Tavis-Cummings model.* In both cases the foundation of the conclusions is given by the Hamiltonians, which has the following form for the Jaynes-Cummings model [10]:

$$\mathcal{H}_{JC} = \mathcal{H}_C + \mathcal{H}_{spin} + \mathcal{H}_{int}, \tag{63}$$

with $\mathcal{H}_C = \hbar\omega_c a^\dagger a$ as the Hamiltonian of the cavity, $\mathcal{H}_{spin} = \frac{1}{2}\hbar\omega_s\sigma_z$ as the Hamiltonian of the spin and $\mathcal{H}_{int} = \vec{\mu} \times \vec{B}$ describing the interaction between the spin and the magnetic field of the cavity. $a^\dagger$ and a denote the creation and annihilation operator and σ_z represents the Pauli spin matrix. The interaction term can also be written as [10]

$$\mathcal{H}_{int} = \hbar g_0(\sigma_+ + \sigma_-)(a + a^\dagger) = \hbar g_0(\sigma_+ a - \sigma_- a^\dagger). \tag{64}$$

Here $g_0 = \frac{\mu_B g B}{2\hbar}$ denotes the single spin coupling rate, with the Bohr magneton μ_B and g the effective coupling constant. $\sigma_\pm$ create or destroy spin exitations. The amplitude of the vacuum magnetic field fluctuation is given by [11]

$$B = \sqrt{\frac{\mu_0\hbar\omega}{2V_m}}, \tag{65}$$

where V_m represents the mode volume. Note that at this point the difference between transmission lines and resonators comes to fruition.

In order to respect losses, one needs to make the spin transition frequency and the cavity frequency complex: $\omega_s \mapsto \omega_s + i\gamma_s$ and $\omega_c \mapsto \omega_c + i\kappa_c$. The loss rate is then proportional to γ_s and κ_r. This leads to the distiction between to regimes regarding the coupling strength. The *weak coupling regime* is defined by the coupling rate being much smaller than the loss rate of the system ($g_0 << \gamma_s, \kappa_r$). Consequently if the spin-resonator interaction is not negligible anymore, the coupling rate is much larger than the loss rate ($g_0 >> \gamma_s + \kappa_r$) [10].
For common values, coupling rates are by a factor of $10^3 - 10^4$ smaller than the loss rates and the interaction is therefore negligible. This problem can be solved by using collective effects of spin ensembles, described by the *Tavis-Cummings model*, which is an extension of the Jaynes-Cumming model. The Hamiltonian is given by [10]

$$\mathcal{H}_{TC} = \hbar\omega_c a^\dagger a + \frac{1}{2}\hbar\omega_s \sum_{i=1}^{N} \sigma_z^i + \sum_{i=1}^{N} g_0^i(\sigma_+ a - \sigma_- a^\dagger). \tag{66}$$

This expression can be simplified by introducing collective spin operators $J_i = \sum_{n=1}^{N} \sigma_i^n$. Assuming all spins couple to the resonator with equal strength g_0, a collective coupling rate can be defined as [10]

$$g_{eff} = \sqrt{\sum_{i=1}^{N} |g_0^i|^2} = g_0\sqrt{N}. \tag{67}$$

Therefore the problem of weak single spin to resonator coupling can be overcome by increasing the number of spins, which leads to an augmentation to coupling rates of in the order of MHz [10].

3 CST simulations

The overall project's aim is to realize a transmission line based quantum memory system, using RE-doped YSO as a dielectric material of a coaxial, coplanar and twin-wire transmission line, all matched to 50 Ω. The input and and output line are both coaxial cables, both matched to 50 Ω. Therefore the inner radius has a fixed ratio to the outer radius of 3.35. For all designs, copper is used as the conducting material. The actual work, was to optimize each configuration regarding the transmission properties, using EM simulations by CST. Important features from this software are the functions *Parameter sweep*, which varies a parameter from a chosen starting to an ending point in a specified number of steps, and *Optimizer*, which optimizes a design with respect to a chosen parameter and goal (e.g. maximizing, minimizing, etc.) by varying a number of parameters in close proximity to their staring values. The first function was therefore used to find out in what region the optimal configuration has to lie in and the latter to figure out the actual optimum. Another important feature is the possibility to set *boundary conditions*. This setting defines what electromagnetic properties the six adjacent faces to the model are having. The two settings that were used are the *open boundary* and *grounded*, the latter served to the conductors carrying the signal and the grounded ones.
Since the coupling rate is dependent on the magnetic field, spins in proximity to each other may experience different coupling rates, depending on the field distribution. So

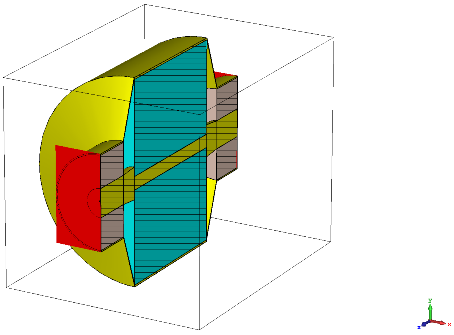

Figure 5: Cross-section in the y-z plane of the coaxial model used in CST.

in order to avoid and minimize perturbation effects from spins on each other, homogeneously distributed EM fields are most favorable. Therefore the power flow, the electric and magnetic fields are evaluated for the final configurations. In the following sections the actual optimization processes are presented.

3.1 Coaxial design

The crystal in the coaxial design is a hollow cylinder of length 10 mm with an inner diameter of 1 mm and an outer diameter of 15 mm, that is filled with an inner conductor and wrapped by an outer conductor that is grounded. The crystal part is connected to the cable by a cone as shown in figure 5. The face with the $-\hat{y}$ normal vector is grounded in order to make the outer conductors grounded. All other boundaries where set to open.

To find the optimal configuration the parameters that were varied are the cone-length l, the inner radius of the cable a, the radius of the inner cone connected to the crystal r and the thickness of the outer conductors of the cable $t1$ and the crystal part $t2$. At first a parameter sweep of l (fig. 6a) has been performed with the following settings: starting value = 1 mm, ending value = 5 mm, step width = 0.5 mm. The most favorable result is obtained at $l = 1.5$ mm, despite not having the highest average S_{21} parameter, but the oscillation is less extreme than for $l = 1$ mm. Subsequently the parameter sweep of a, from 0.5 mm to 1.6 mm with a step width of 0.1 mm, was made. The variation did not change the curve for S_{21} much, besides enhancing or lowering the oscillation. Therefore the results are not shown in a figure, but the best transmission was achieved for an inner radius of 1.0 mm. Afterwards r was varied from 0.5 mm to 1.5 mm in steps of 0.1 mm. As shown in figure 16 the best transmission is given for $r = 1.2$ mm. Varying the thickness of the outer conductors only changed the oscillation strength. The best settings lied at $t1 = 0.15$ mm and $t2 = 0.3$ mm. Afterwards the final improvement was executed by using the *Optimizer* function with the goal to maximize the lowest S_{21} value. The predetermined parameters were used as starting points. Here the outer radius of the in-/output cable b was varied as well, in order to make up for possible inaccuracies in the calculation of the b/a ratio. The optimized parameters are presented in the tabular 5.

Variable	l	r	a	b	t1	t2
Value [mm]	1.466	1.202	1.064	3.436	0.098	0.138

Table 5: Optimized parameters for the coaxial design.

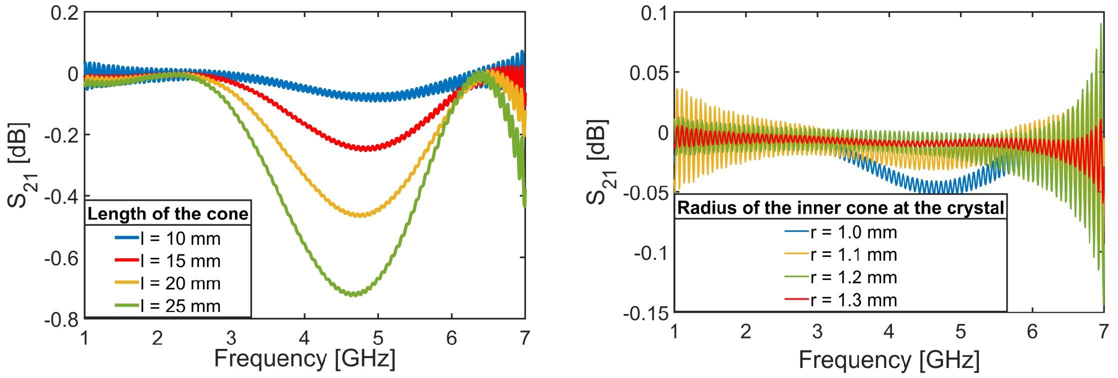

(a)

(b)

Figure 6: Results of the parameter sweeps for l in a) and a in b) with the best result shown by the red line.

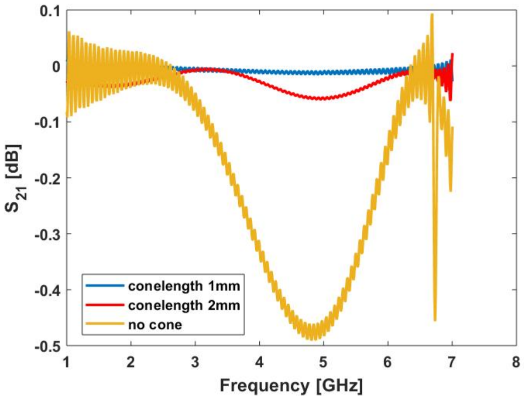

Figure 7: Comparison of the coaxial design with and without a cone.

Another way to connect the cable and the central part, is to leave out the cone and to make a "face to face" connection between both components. However, this configuration proved to be worse than the previous one as shown in figure 7.

Now taking a look at the power flow, the distribution diminishes as expected exponentially with the radius. The power flow is modeled along the x-axis and negative y-axis in the pictures 8a and 8b. As one can see, the power flow depends not just on the radius but also on the angle, as the peaks have a difference in amplitude by a factor two. This can be explained by anisotropic effects of the YSO. For the sake of visualization, the first mode of the electric and magnetic fields are shown in the images 9a and 9b.

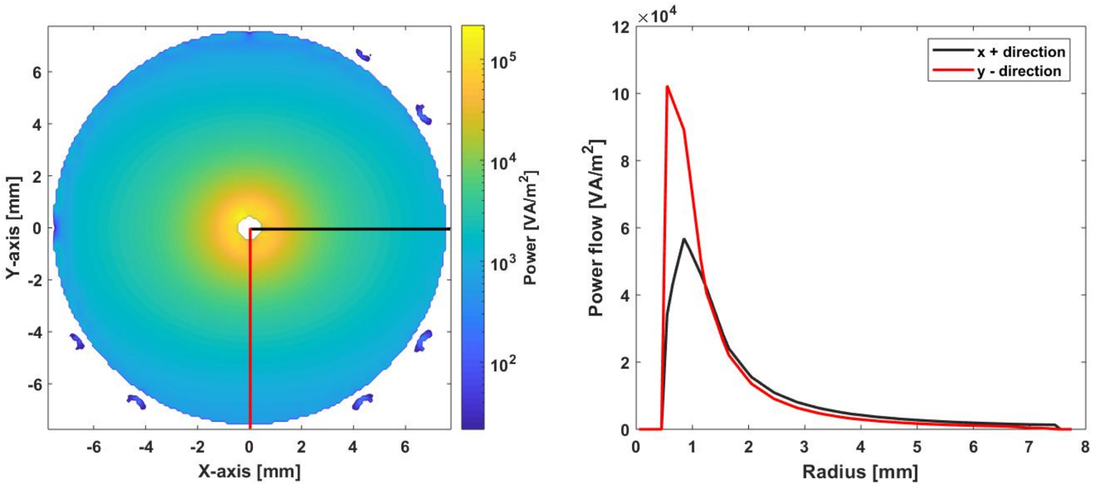

(a) (b)

Figure 8: Illustration of the powerflow in the x-y plane (a), with the exact graphs along the two indicated directions (b).

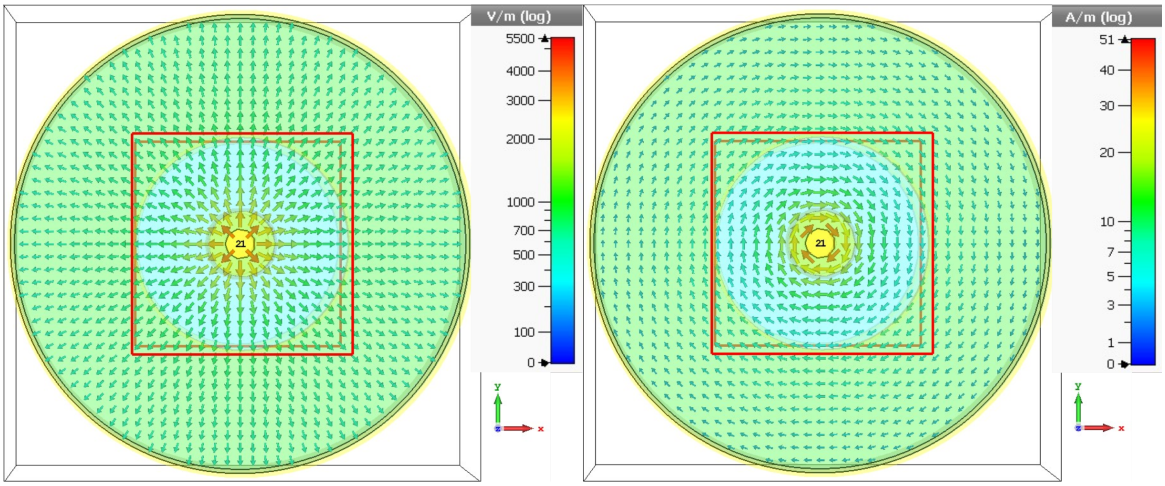

(a) (b)

Figure 9: Illustration of the electric (a) and magnetic field (b) in the x-y plane.

3.2 Coplanar design

For the coplanar design, the crystal has a cuboidal shape of width 7 mm, height 3 mm and length 50 mm. Copper plates of thickness t and width w are placed on top and on the bottom of the crystal, where the bottom is grounded. Two coaxial cables are connected to the front and back in a distance d, while the inner conductors are linked to the upper plate and outer conductors to the bottom plate as shown in picture 10. The boundary conditions were the same as in the coaxial case.

The parameters varied in this configuration are t, w, d, the inner radius a of the coaxial cable and the height h at which the cable center is put compared to the middle of the crystal. The first parameter sweep was performed on the plate widths, starting at 2.0 mm going with a step width of 0.2 mm to 4.0 mm. The best value was reached at 3.2 mm as illustrated in the plot of figure 11a. To be assured that this is indeed the

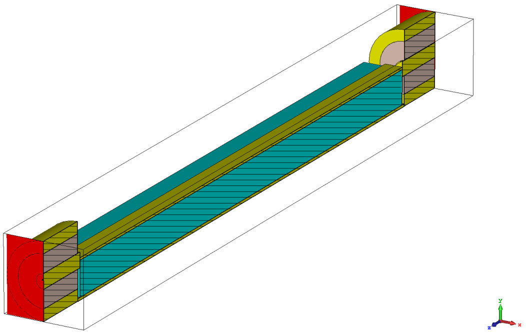

Figure 10: Cross-section in th y-z plane of the coplanar model used in CST.

Variable	w	h	t_1	a	b	t_2	d
Value [mm]	3.113	1.523	0.199	0.643	2.227	0.995	0.334

Table 6: Optimized parameters for the coaxial design.

region for the optimal width, the result was compared with a plate that covers the hole surface ($w = 7$ mm). The second parameter sweep was performed on the height of the cable h from 1 mm to 1.7 mm, with a step width of 0.1 mm (fig. 11b). The best setting is given at $h = 1.5$ mm which is slightly more favorable than $h = 1.6$ mm because it has higher S_{21} values in the range of 1.5 GHz - 4 GHz and a similar trajectory for the higher frequencies. So the center of the cable is approximately at the top edge of the crystal. The next step was the variation of the plate thickness as illustrated in figure 11c. One can observe a trend of increasing transmission with decreasing thickness, up to a certain point between $t = 0.1$ mm and $t = 0.2$ mm where some disturbance effects seem to gain dominance, as indicated by the dip at 2.3 GHz. Afterwards a parametric sweep on a has been made, with the following settings: Starting value: 0.40 mm, final value: 0.90 mm, step width: 0.05 mm. The best setting is given for $a = 0.65$ mm (fig. 12a). Changing the thickness of the outer conductors t_2 from the cables did not make a big difference regarding the transmission, however $t_2 = 1$ mm was the slightly better setting. The last parameter sweep was performed on the gap between the cable and the crystal. The results are illustrated in figure 12b. Finally the entire design was optimized, with the optimized set of parameters listed in table 6.

Taking a look at the power flow shown in picture 13a, the distribution matches with the expectation around the upper conductor, but one might wonder why the power is that high on both sides of the lower conductor. This can be explained by the boundary conditions chosen in CST, where the $-\hat{y}$-plane is set as ground. Since the power in between both plates is most interesting, it is illustrated in figure 13b along the black line shown in the power flow picture (fig. 13a). For the sake of illustration the electric and magnetic field modes are shown in images 14a and 14b.

3.3 Twinwire

For the twinwire design the crystal has a length of 10 mm, width of 5 mm and height of 3 mm with two holes of radius 0.5 mm in distance 2 mm from each other. Both holes are filled with wires that are connected to coaxial cable on both sides. The right wire is linked with the inner conductor of the cable and the outer conductors are attached to

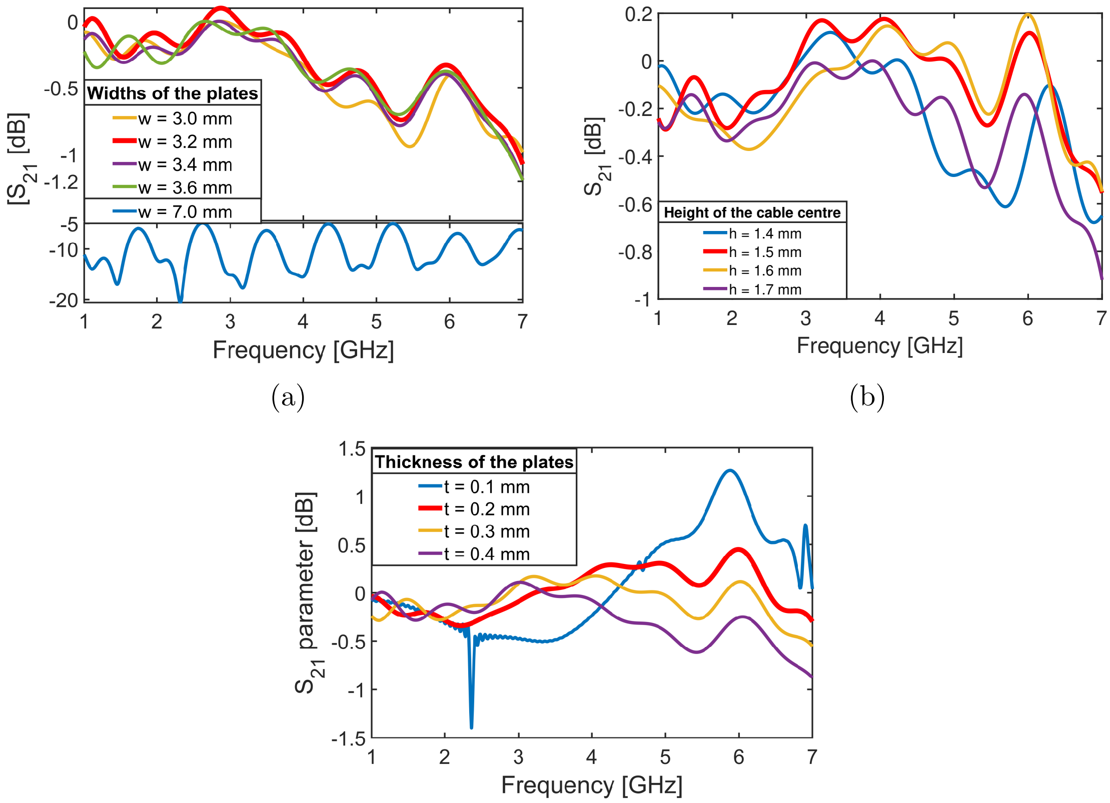

(a)

(b)

(c)

Figure 11: Parameter sweeps of the platewidths w (a), the height of the cable h (b) and the thickness of the plates t (c).

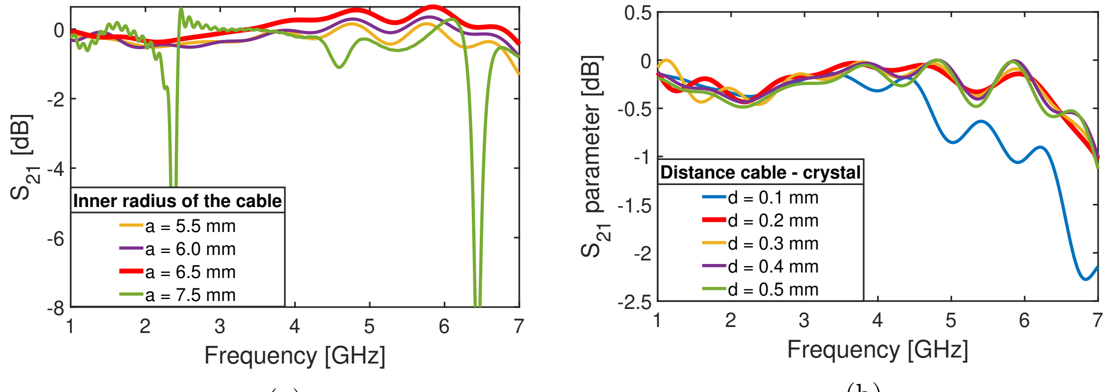

(a)

(b)

Figure 12: parameter sweeps for the inner radius of the cables a (a) and the distance between the cables and the crystal d (b).

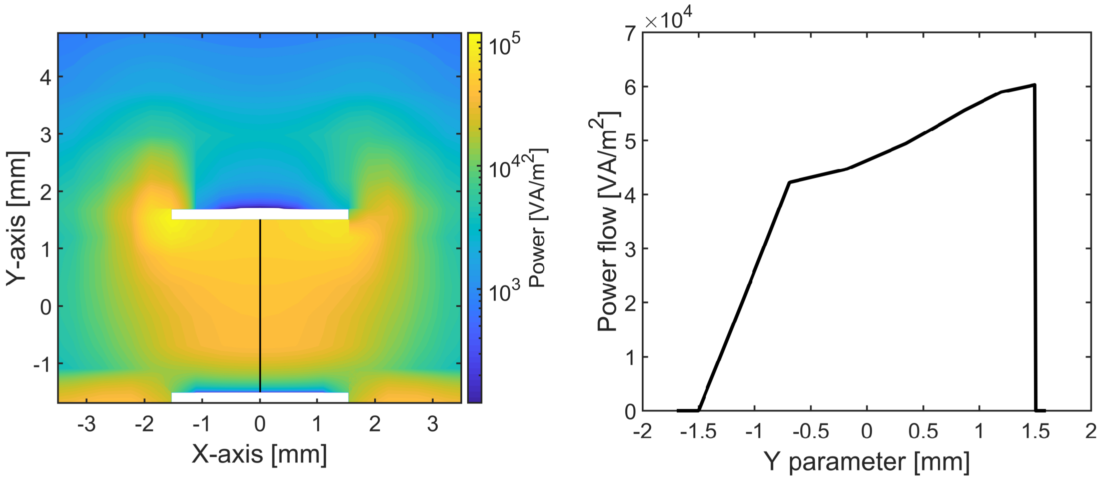

(a) (b)

Figure 13: Powerflow of the coplanar design in the x-y plane (a) and the exact graph between the two conductors indicated by the black line in a (b).

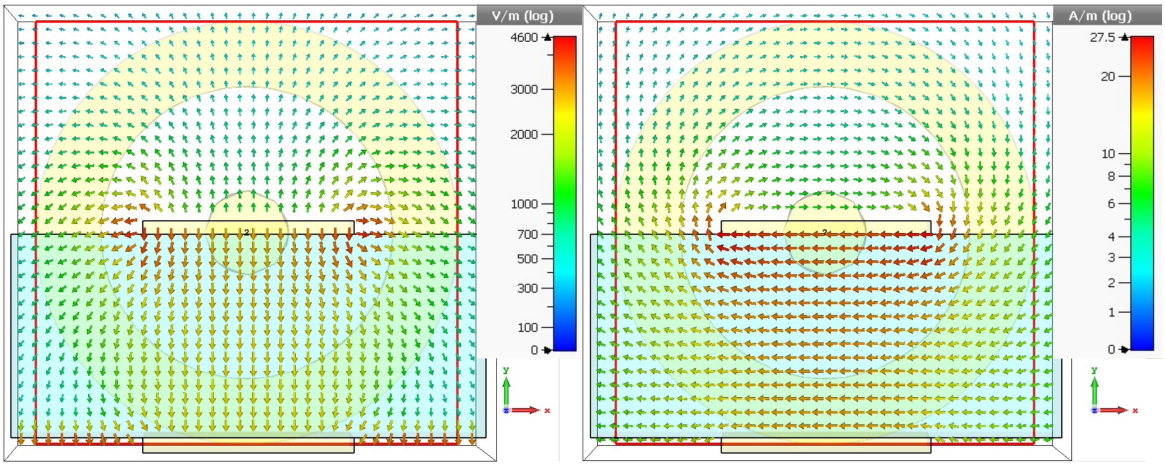

(a) (b)

Figure 14: Electric (a) and magnetic (b) fields for the coplanar design in the x-y plane

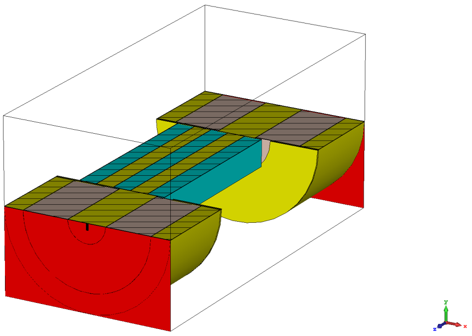

Figure 15: Caption

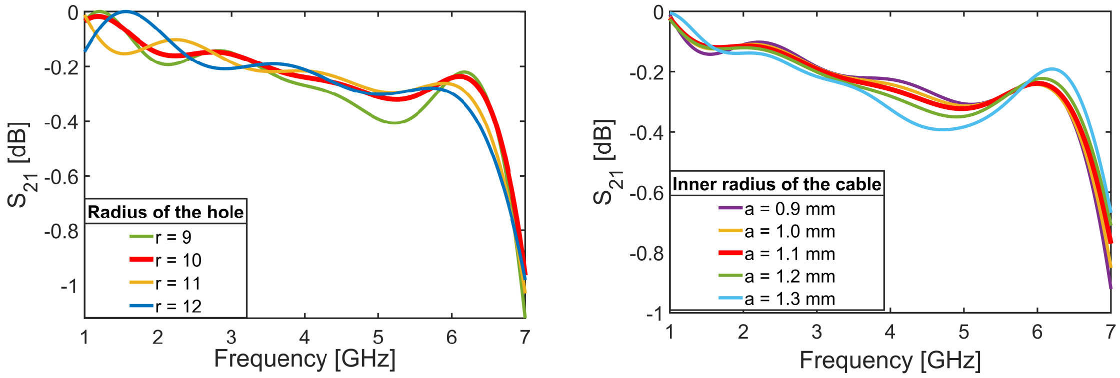

(a) (b)

Figure 16: Parameter sweeps for r (a) and a (b)

the left wire with a circular plate with a hole in the middle (fig. 15). The parameters that were varied are the inner radius of the coaxial cable a, the radius difference between the hole and the inner conductor of the cable dr, the thickness of the outer conductor t and the distance between the crystal and the cable d. d is therefore the thickness of plate as well. The first parametric sweep was performed on the size of the hole, with the following settings: starting value 0.9 mm, ending value 2.3 mm, step width 0.1 mm. The result is presented in figure 16a. As shown, the best value is given for $r = 1.8$ mm. Afterwards the inner radius of the cable was varied, starting at 0.5 mm, going up to 1.5 mm in steps of 0.1 mm. The most favorable transmission is obtained for 1.1 mm, making a compromise between the highest minimum and the highest average (fig. 16b). Changing d and t only changed the curve very slightly, therefore the sweeps are not shown as graphs. The best setting are $d = 0.1$ mm and $t = 1.1$ mm. Since all parameters where varied, the final optimization is determined by the *optimizer*. The results are listed in table 7.

Taking a look at the power flow, one can see that it is very strong in the region between both wires, but weakens quickly outside as shown in fig. 17a. A good property

Variable	a	b	t	dr	d
Value [mm]	0.99	4.054	1.21	1.1	0.091

Table 7: Optimized parameters for the twinwire design.

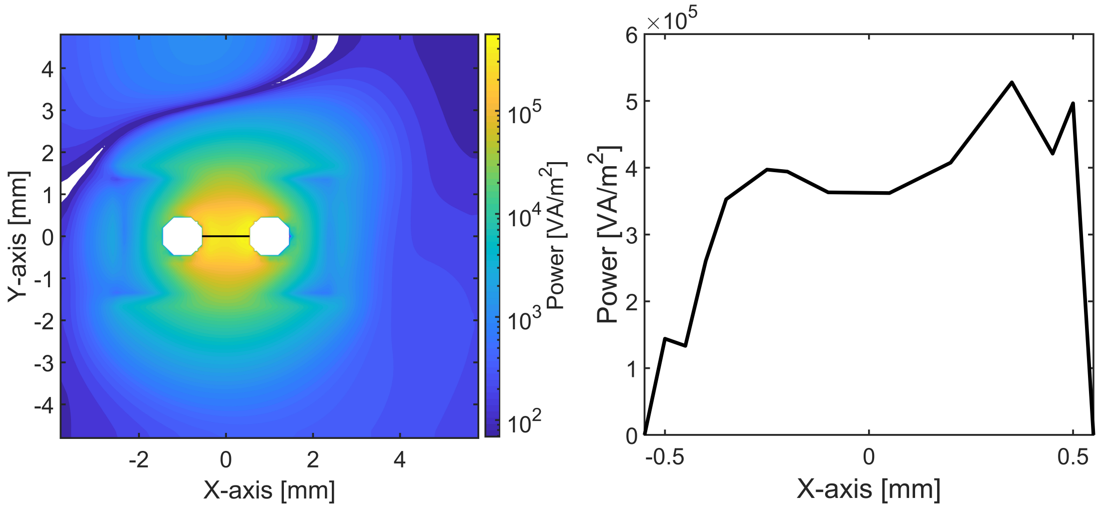

(a) (b)

Figure 17: Power flow for the twinwire design in the x-y plane (a) and the exact graph between the conductors (b).

is that the power flow is rather consistent along the black line between the conductors (fig. 17b). As indicated, the EM fields are very string in the middle region with maxima at approximately 10 500 V/m and 71.5 A/m. The disadvantage in this design is that only the field propagation is only homogeneous and strong between the wires and therefore that is the only region that can be operated at.

4 Conclusion

In order to figure out the best design of the three, there are different sides that need to be considered. The simplest one is the comparison of the impedance, average transmission and reflection (tab. 8). Here, the twinwire has the worst values for all three properties, as its impedance is over 15% higher than 50 Ω which complicates the connection to standard cables and its average transmission is one order of magnitude worse than the other designs.

The impedance for the coplanar design, on the other hand, matches the desired 50 Ω almost perfectly. It has very good transmission as well, as it is the only one with a positive average S_{21} parameter. The expectation would be that it has the least reflection too, but counter intuitively the lowest mean S_{11} parameter is obtained in the coaxial case.

Diving deeper in the comparison the exact S_{21} curves can be analyzed (fig. 19). Here the coaxial design has clearly the most consistent transmission, which is favorable on one hand, but on the other hand the curve oscillates with varying amplitude which is generally not so good, since slight inaccuracies in the frequency lead to stronger changes in the magnetic fields and therefore to different coupling rates. The highest value for S_{21} is obtained for the coplanar design, but it also has the largest difference between the maximum and minimum of the curve which needs to be taken into account in the storage protocols. The twinwire design has worse transmission than the other two, but it is rather consistent between 1.5 and 7 GHZ.

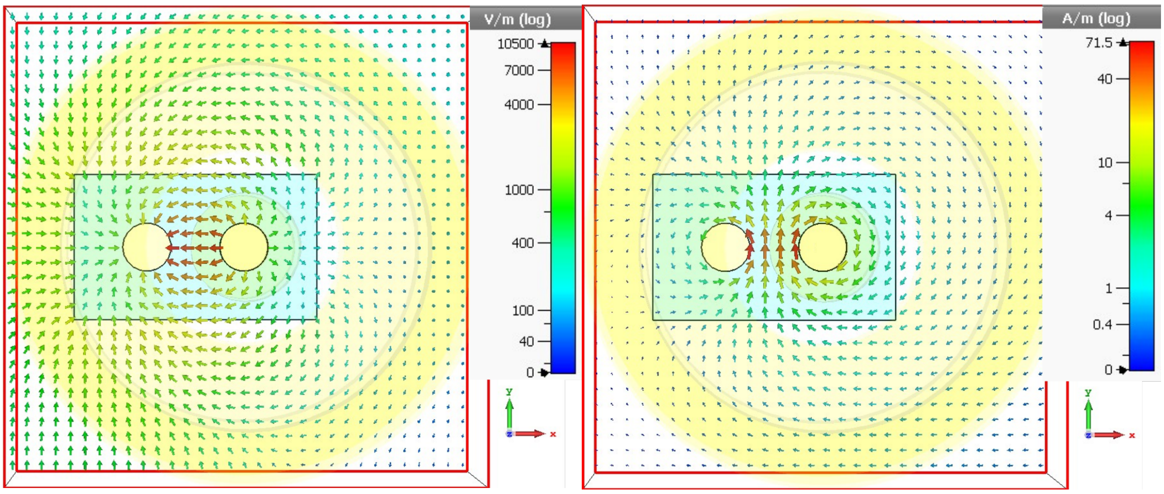

(a) (b)

Figure 18: Electric (a) and magnetic (b) fields for the twinwire design in the x-y plane

design	S_{21} [dB]	S_{11} [dB]	Z [Ω]
Coaxial	-0.01006	-34.80208	48.469773
Coplanar	0.04626	-24.33420	50.000502
Twinwire	-0.33730	-18.84199	58.33832

Table 8: Comparison of the most important TL parameters for all three designs

Comparing the EM fields, the most homogeneous field propagation is given for the coplanar design between the plates, as the field lines are all parallel to each other and the strength is rather consistent, but rather weak compared to the other two models (fig. 14a, 14b). The field lines are very homogeneous in the coaxial case as well, but due to the anisotropy of the YSO the strength varies strongly for different directions, as indicated by the powerflow (fig. 8a, 8b). Additionaly the field strengths diminish quickly with increasing distance from the center. Similarly the EM fields between the to conductors in the twinwire design are the strongest out of all three, but weaken strongly outside of that region (fig. 18a, 18b).

The last point that needs to be taken into account is the complexity of the design. Here the coaxial and twinwire designs are much easier to implement in external circuitry due to there smaller dimensions.

Concluding one can say that all three models have their own advantages and which one is best suited depends on the actual application, but the coaxial and coplanar design are probably better for most tasks then the twinwire design.

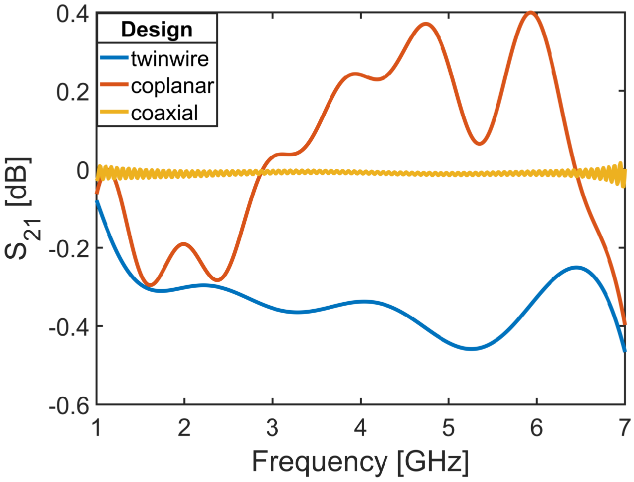

Figure 19: S_{21} curves for all three optimized designs

References

[1] Y. Alexeev, D. Bacon, K. R. Brown, R. Calderbank, L. D. Carr, F. T. Chong, B. DeMarco, D. Englund, E. Farhi, B. Fefferman, A. V. Gorshkov, A. Houck, J. Kim, S. Kimmel, M. Lange, S. Lloyd, M. D. Lukin, D. Maslov, P. Maunz, C. Monroe, J. Preskill, M. Roetteler, M. J. Savage, and J. Thompson, “Quantum computer systems for scientific discovery,” *PRX Quantum*, vol. 2, p. 017001, Feb 2021.

[2] A. Kinos, D. Hunger, R. Kolesov, K. Mølmer, H. de Riedmatten, P. Goldner, A. Tallaire, L. Morvan, P. Berger, S. Welinski, K. Karrai, L. Rippe, S. Kröll, and A. Walther, “Roadmap for rare-earth quantum computing,” 2021.

[3] G. Kurizki, P. Bertet, Y. Kubo, K. Mølmer, D. Petrosyan, P. Rabl, and J. Schmiedmayer, “Quantum technologies with hybrid systems,” *Proceedings of the National Academy of Sciences*, vol. 112, no. 13, pp. 3866–3873, 2015.

[4] C. Simon, M. Afzelius, J. Appel, A. Boyer de la Giroday, S. J. Dewhurst, N. Gisin, C. Y. Hu, F. Jelezko, S. Kröll, M. J. H., J. Nunn, E. S. Polzik, J. G. Rarity, H. D. Riedmatten, W. Rosenfeld, A. J. Shields, N. Sköld, R. M. Stevenson, R. Thew, I. A. Walmsley, M. C. Weber, H. Weinfurter, J. Wrachtrup, and R. J. Young, “Quantum memories,” *The European Physical Journal D*, vol. 58, pp. 1–22, 2010.

[5] “https://www.spektrum.de/lexikon/physik/stark-effekt/13753.”

[6] “https://upload.wikimedia.org/wikipedia/commons/thumb/a/af/structurenvcenter.jpg/330px-structurenvcenter.jpg.”

[7] C. Liu, Z. Dutton, C. H. Behroozi, and L. V. Hau, “Observation of coherent optical information storage in an atomic medium using halted light pulses,” *Nature*, vol. 409, p. 490–493, 2001.

[8] D. M. Pozar, *Microwave Engineering fourth edition*. John Wiley Sons, Inc., 2011.

[9] J. K. N. C. Carvalho, J-M. Le Floch and M. E. Tobar, “Multi-mode technique for the determination of the biaxial y_2sio_5 permittivity tensor from 300 k to 6 k,” *Applied Physics Letters*, vol. 106, 2010.

[10] S. Weichselbaumer, *Spin Dynamics in Strongly Coupled Spin-Photon Hybrid Systems.* PhD thesis, 2020.

[11] S. Probst, *Hybrid quantum system based on rare earth doped crystals.* KIT Scientific Publishing, 2016.